nature electronics

ARTICLES

https://doi.org/10.1038/s41928-022-00755-5

Check for updates

Graphene charge-injection photodetectors

Wei Liu[1,9], Jianhang Lv[1,9], Li Peng[2,9], Hongwei Guo[1,9], Chen Liu[1], Yilun Liu[1], Wei Li[1], Lingfei Li[1], Lixiang Liu[1], Peiqi Wang[3], Srikrishna Chanakya Bodepudi[1], Khurram Shehzad[1], Guohua Hu[4], Kaihui Liu[5], Zhipei Sun[6], Tawfique Hasan[7], Yang Xu[1]✉, Xiaomu Wang[8]✉, Chao Gao[2]✉, Bin Yu[1]✉ and Xiangfeng Duan[3]✉

Charge-coupled devices are widely used imaging technologies. However, their speed is limited due to the complex readout process, which involves sequential charge transfer between wells, and their spectral bandwidth is limited due to the absorption limitations of silicon. Here we report graphene charge-injection photodetectors. The devices have a deep-depletion silicon well for charge integration, single-layer graphene for non-destructive direct readout and multilayer graphene for infrared photocharge injection. The photodetectors offer broadband imaging from ultraviolet (around 375 nm) to mid-infrared (around 3.8 μm), a conversion gain of 700 pA per electron, a responsivity above 0.1 A W^{-1} in the infrared region and a fast response time under 1 μs.

Charge-coupled devices (CCD) and complementary metal–oxide–semiconductor (CMOS) technology are widely used in high-end imaging applications[1–9]. Both have their own merits and limitations. The simple metal–oxide–semiconductor photogate pixel and charge integration function in CCDs results in a high fill factor (FF), high sensitivity and low noise[10,11], but the serial charge transfer between wells requires complex multiphase biasing/clocking[11,12], limiting the readout speed. In CMOS sensors, the independent pixel structure allows random access, simple clocking, high-speed parallel readout, natural anti-blooming and monolithic integration with processing circuitry[11,13–15]. However, CMOS usually has a lower FF and higher noise than CCD due to the relatively complex active pixel sensor structure and subsequent circuitry[13].

Both silicon-based CCD and CMOS imagers are also generally not applicable beyond the visible range due to the intrinsic bandgap absorption limit of silicon. This is usually overcome through the heterogeneous integration of metal silicide Schottky barrier detectors[16–18]; however, these have a complicated structure, low FF and high cost, and they require low-temperature operation. The integration of narrow-gap III–V or II–VI semiconductors can extend the spectral response regime[19,20], but this is technically challenging, costly and typically limited to the near-infrared (NIR) regime. Further expansion into the mid-infrared (MIR) regime[21] has been a persistent challenge due to the intrinsic thermal noise in narrow-gap semiconductors. Graphene is of potential use in imaging devices due to its monolithic integration with CMOS[22–25], strong field effect for electrostatic photogating[26–28] and broadband absorption spectrum[29–33]. Incorporating graphene into silicon-based image sensors could thus be used to improve the responsivity and spectral performance.

In this Article, we report graphene charge-injection (GCI) photodetectors that combine the charge integration feature of CCD and the independent pixel structure of CMOS. The photodetector consists of a deep-depletion SiO_2/Si well sandwiched between single-layer graphene (SLG) on top of the structure (for direct field-effect readout) and multilayer graphene (MLG) at the bottom (for broadband charge injection) (Fig. 1a). The MLG, composed of weakly coupled graphene layers, is able to enhance the photoresponse up to the MIR range. The optical properties of graphene, such as broadband optical absorption and efficient hot carrier generation, are preserved in the MLG due to its weak interlayer interaction. Our detector exhibits high sensitivity (>0.1 A W^{-1} in the infrared (IR)) and high speed (<1 μs), as well as broadband imaging (ultraviolet to MIR at room temperature), high linearity, high FF, low noise and low cost.

Structure of GCI photodetectors. Three functionalities are integrated into the GCI to broaden the detection bandwidth and simplify the readout process (Fig. 1b). First, a Schottky junction is formed between the silicon and MLG layer. Hot holes induced in the MLG by IR light are injected into silicon (n type) under the electrical field of a gate voltage (V_g) via photothermionic (PTI) emission[34]. The MLG is experimentally verified to have larger absorption than silicon in a broad spectral range (around 40% from 2.5 to 5.0 μm; Supplementary Fig. 1). Visible light is absorbed by silicon in the front-illumination configuration, whereas IR light (where silicon is transparent) is mainly absorbed by the MLG layer. Second, a deep-depletion well is formed in the SiO_2/Si interface under the voltage pulse, which stores and integrates photocharges. Third, the SLG on top of the oxide is used for direct and non-destructive readout of the carriers stored in the deep-depletion well, by the

[1]School of Micro-Nano Electronics, ZJU-Hangzhou Global Scientific and Technological Innovation Center, State Key Laboratory of Silicon Materials, ZJU-UIUC Joint Institute, Zhejiang University, Hangzhou, China. [2]Department of Polymer Science and Engineering, MOE Key Laboratory of Macromolecular Synthesis and Functionalization, Key Laboratory of Adsorption and Separation Materials & Technologies of Zhejiang Province, Zhejiang University, Hangzhou, China. [3]Department of Chemistry and Biochemistry, California Nanosystems Institute, University of California, Los Angeles, CA, USA. [4]Department of Electronic Engineering, The Chinese University of Hong Kong, Shatin, China. [5]State Key Laboratory for Mesoscopic Physics, School of Physics, Peking University, Beijing, China. [6]Department of Electronics and Nanoengineering and Department of Applied Physics, Aalto University, Espoo, Finland. [7]Cambridge Graphene Centre, University of Cambridge, Cambridge, UK. [8]National Laboratory of Solid State Microstructures, School of Electronic Science and Engineering, Collaborative Innovation Center of Advanced Microstructure, Nanjing University, Nanjing, China. [9]These authors contributed equally: Wei Liu, Jianhang Lv, Li Peng, Hongwei Guo. ✉e-mail: yangxu-isee@zju.edu.cn; xiaomu.wang@nju.edu.cn; chaogao@zju.edu.cn; yu-bin@zju.edu.cn; xduan@chem.ucla.edu

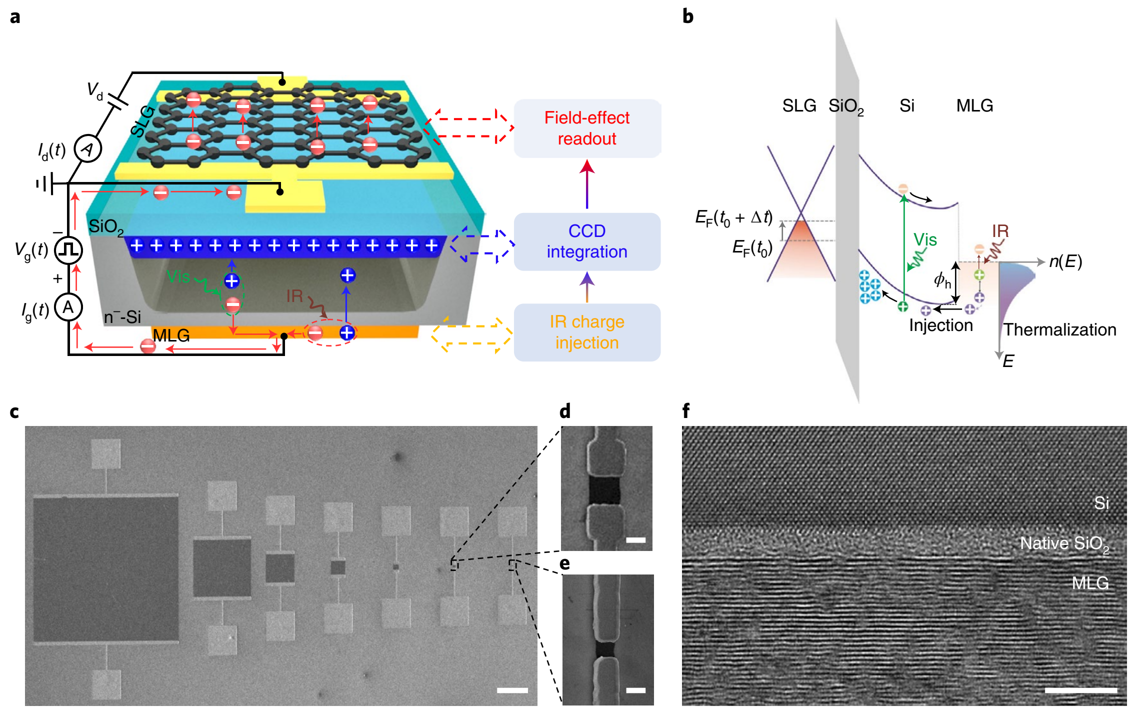

Fig. 1 | Device structure and band diagram of GCI. a, Schematic of GCI consisting of a deep-depletion silicon well for charge integration, SLG for non-destructive direct readout and MLG layer for IR photocharge injection. Visible light is absorbed by the silicon in the front illumination configuration, whereas IR light is mainly absorbed by the MLG layer. **b**, Band diagram of the GCI. The holes in green are excited under visible light, and those in purple are thermalized hot carriers that can be injected into silicon from the long thermal tail of the hot carrier distribution. The holes in blue are integrated in the potential well. E_F represents the Fermi level of Si. GCI device is under non-equilibrium state at $t = t_0$ and under equilibrium state at certain time $t = t_0 + \Delta t$. **c**, SEM image of the GCI pixels with different sizes. The length and width of the pixel are 500, 200, 100, 50, 20, 10 and 5 μm. **d**, Enlarged image of the 10 μm pixel. **e**, Enlarged image of 5 μm pixel. **f**, Cross-sectional TEM image of the MLG/Si Schottky junction. Scale bars in **c**–**f** are 100 μm, 5 μm, 5 μm and 5 nm, respectively.

photogating effect caused by the strong field effect of the SLG. However, it should be noted that the photogating in our device is essentially a depletion well gating effect.

Scanning electron microscopy (SEM) images of GCI pixels with different sizes (Fig. 1c–e and Supplementary Fig. 2) demonstrate that the GCI pixels can be scaled and potentially integrated at high density. A cross-sectional transmission electron microscopy (TEM) image (Fig. 1f) shows the high-quality interface of the MLG/Si junction, which is due to the use of a van der Waals integration strategy[35,36].

In the traditional CCD structure, multiphase clock pulses are applied to the pixels to serially transfer photocharges to the readout circuit. Such a multiphase serial charge transfer is notably not necessary in our GCI as direct real-time charge readout can be realized from each potential well via a highly charge-sensitive photogating effect of the SLG. Specifically, the photo- and thermally generated holes are integrated in the deep-depletion well of silicon, whereas the same number of electrons are imaged in the SLG through capacitive coupling, resulting in a real-time change in drain current I_d of the SLG (Fig. 1a,b). This real-time monitoring of charge in the GCI has several advantages over traditional CCD image sensors. First, the charges in the potential well are directly read out, avoiding serial charge transfer between the adjacent wells required in traditional CCDs. Second, the charge readout and charge integration process are independent, that is, the readout operation does not interrupt the charge integration process (the readout is non-destructive). Third, the photogating effect from the SLG, where the output signal of the GCI is amplified by the field-effect modulation of the graphene sensor with a high transconductance gain, contributes to high sensitivity and fast response time. The use of the photogating effect to improve both sensitivity and speed has been reported previously[37,38], which demonstrated the combination of photosensing and charge storage techniques. Here we advance this strategy by integrating a monolayer readout transistor with a deep-depleted potential well, which substantially improves the sensitivity via the photocharge integration effect in a controllable manner.

Charge integration and non-destructive direct readout. We first demonstrate the charge integration and non-destructive direct readout in the GCI with a moderately doped wafer (n type; resistivity of Si, 1–10 Ω cm; thickness of SiO_2, 15 nm) in the visible range. To create the potential well for charge integration, we use a fast sweeping ramp (10 V s^{-1}) to drive the silicon into the deep-depletion state, which can be seen from the continually decreasing capacitance as V_g increases under the dark condition (Fig. 2a, with no light illumination). Under light illumination (532 nm), the photoholes fill the deep-depletion well, reducing the depletion depth and increasing the capacitance value, in a way similar to traditional CCDs. To drive the silicon more efficiently into a non-equilibrium deep-depletion state, we use a transit pulse voltage, which has a very large sweep rate compared with the ramp voltage (Supplementary Figs. 3 and 4 and Supplementary Text 2). The holes integrated in the well image the same number of electrons in the SLG readout channel through capacitive coupling, therefore leading to a decrease in conductivity in the initially p-doped SLG channel (Fig. 2b). In this way, the number of photoholes integrated in the deep-depletion well is directly monitored in real time by the drain current I_d of the SLG. The corresponding static testing is shown in Supplementary Fig. 5. A reset

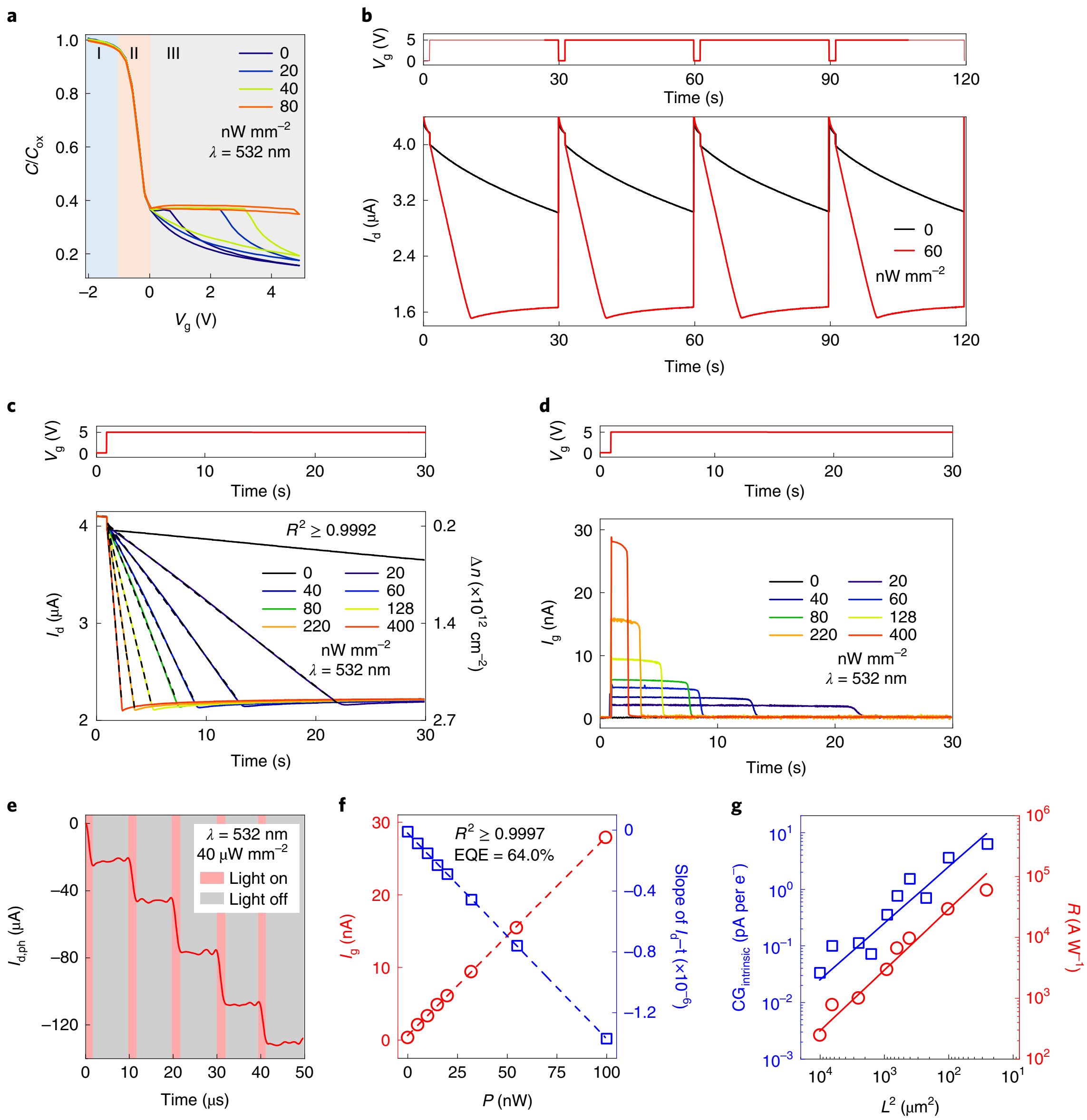

Fig. 2 | Characterization of GCI. **a**, Normalized Capacitance-Voltage (CV) (100 kHz) of the GCI pixels at different illumination powers (wavelength, 532 nm). Gate voltage (defined to be positive on Si) is swept from −2 to 5 V and then swept back to −2 V at a speed of 10 V s^{-1}. Oxide capacitance C_{ox} = 3.5 × 10^{-4} pF μm^{-2}. Regions I, II and III represent the accumulation, depletion and deep-depletion/inversion regime, respectively. **b**, I_d–t characteristic under periodic gate-voltage pulses in dark and illumination (60 nW mm^{-2}) conditions. Top, V_g profile; bottom, I_d curves. **c**, Real-time monitoring of I_d–t under V_g pulse and 532 nm laser illumination. The dashed lines are the linear fits according to equation (1). The variation in carrier density in the SLG channel is shown in the right axis. **d**, Real-time monitoring of I_g–t under the same conditions as **c**. The drain voltage V_d in **b**, **c** and **d** is 10 mV. **e**, Photocurrent under 100 kHz pulsed laser. The laser is turned on and off in the red and grey regions, respectively. Drain bias V_d = 1.5 V. **f**, I_g (red circle) and slope of I_d–t (blue square) as a function of laser power and their linear fitting (red and blue dashed lines, respectively). **g**, Scaling effect of GCI: the intrinsic conversion gain (blue square) and responsivity (red circle) as a function of L^2. The pixel size equals L^2 in the square-shaped pixels. The blue and red lines are theoretical calculations.

signal (V_g = 0) empties the potential well and drives the silicon back to an equilibrium state, ready for the next cycle of charge integration (Fig. 2b). It is worth noting that the pulsed V_g is essential to create a deep-depletion potential well for charge integration; otherwise, the device will quickly go back to the equilibrium state and have a small well capacity[37,38]. Since the depletion layer is controlled by the pulsed V_g, the doping level of silicon has a little influence on the performance in the visible-light region. For example, we demonstrate that our GCI can work in the visible region with low-doped silicon (resistivity, 10 kΩ cm; Supplementary Fig. 5c,d).

The change in I_d originates from photohole generation and integration in the deep-depletion well, and the same number of electrons is imaged in the SLG channel:

$$I_d = \left(n_0 - \frac{P\eta t}{h\nu A} - g_{TH}t\right) q\mu V_d \frac{W}{L}, \quad (1)$$

where n_0 and μ are the initial carrier density and mobility in SLG, respectively; P and ν are the light power and photon frequency, respectively; g_{TH} is the thermal generation rate in silicon, η is the external quantum efficiency (EQE), h is the Planck's constant and q is the elemental charge; and A, L and W are the area, length and width of the pixel, respectively. The $P\eta$ value (equation (1)) can be written as $P_{Si}\eta_{exc}+P_{MLG}\eta_{inj}$, where P_{Si} and P_{MLG} are the illumination power absorbed by silicon and MLG, respectively, and η_{exc} and η_{inj} are the quantum efficiency in Si and charge-injection efficiency from MLG to silicon, respectively. Under visible-light illumination, $P_{MLG}=0$ because the top-illuminated light is completely absorbed by silicon. Meanwhile, the photoelectrons drift outside the deep-depletion well, contributing to the charging current I_g:

$$I_g = \frac{P}{h\nu} q\eta + g_{TH} qA. \quad (2)$$

The experimental results show excellent agreement with the above equations (Fig. 2c,d). Under the dark condition, the I_d–t curve in the pulse region shows little change since no carriers fill the potential well in the dark, except for those from thermal carrier generation. The thermal carrier generation rate is slow in silicon (dark relaxation time of ~200 s at room temperature) (Supplementary Fig. 6). Under the light-illumination condition, the photoholes keep on filling the deep-depletion well until the well is full, causing the I_d–t values of SLG to first decrease (linear region) and then saturate (saturation region) within a relatively short time. This large difference in I_d between the illumination and dark conditions results from the charge integration effect in the deep-depletion well and high transconductance gain in the GCI, both of which contribute to the high sensitivity in our GCI. The corresponding I_g values under dark and light conditions are shown in Fig. 2d, remaining at a non-zero constant value before the well is full. Charge integration and real-time monitoring are also demonstrated with laser pulses, as shown by the step-like waveform of the drain photocurrent $I_{d,ph}$–t (Fig. 2e). Multipulse charge integration under optical stimulations shows that our GCI can potentially work as a neuromorphic vision sensor with the preprocessing-in-image-sensor function[39]. The GCI also has the potential for multivalued logic technologies as it can output several current levels depending on the incident-light illumination.

The GCI shows high linearity in the photocharge integration and readout process (Fig. 2c,f), which is necessary for use in imaging applications. Due to the negligible thermal generation rate, the I_d (P, t) value in equation (1) incorporates two features of linearity, which can also be seen in the experimental I_d (P)–t under the light condition. First, I_d linearly decreases with time before saturation (variance of the least-squares fitting $R^2 \geq 0.9992$; Fig. 2c). Second, the slope of I_d–t (photocharge generation rate) linearly increases with the light power ($R^2 \geq 0.9997$; Fig. 2f, blue curve), as well as the slope of the I_g–P data ($R^2 \geq 0.9997$; Fig. 2f, red curve). We extract a consistent EQE value of 64.0% of the GCI from equations (1) and (2). We also extract a thermal carrier generation rate g_{TH} of 312 e$^-$ μm^{-2} s^{-1} in silicon at room temperature, which is slow enough to enable a long integration time (Supplementary Fig. 6).

In addition to the linearity and EQE, other figures of merit in our GCI are comparable to state-of-the-art image sensors (Fig. 2g and Supplementary Table 1). The high transconductance (equation (1)) in the GCI offer a high gain mechanism for the photocharges in the potential well, contributing to high sensitivity. Importantly, this gain based on the transconductance in our GCI is distinct from traditional photoconductive gain. Photoconductive gain usually relies on traps and has low speed[40]. The gain in our GCI is enabled by the high transconductance gain of the SLG FET sensor and thus ensures high sensitivity and fast time response.

The intrinsic conversion gain ($CG_{intrinsic}$), defined as the output current with a single excitation of photocharge, reaches ~7 pA per electron under a V_d value of 10 mV. Further, this value can be improved to 700 pA per electron by increasing V_d to 1 V. An external CG value of ~7 μV per electron can be obtained using a transimpedance amplifier with a gain of 10^4. We also obtain a high responsivity (R) of 6×10^4 A W^{-1} in the 5 μm × 5 μm (square) pixel in the visible range. Here $CG_{intrinsic}$ ($q\mu V_d/L^2$) and R ($qt\eta\mu V_d/h\nu L^2$) values can be independently improved through the mobility, drain voltage and pixel channel length without influencing the full well capacity, offering considerable design space for further improving the sensitivity (Fig. 2g, Supplementary Fig. 7 and Supplementary Text 5). Simultaneously, we obtain a rapid response time of less than 1 μs in the GCI (Fig. 2e), which is limited by the speed of the laser. It is worth noting that the long time needed for I_d to reach saturation (Fig. 2b,c) is not the response time of the device but the integration time to fully fill the potential well. In practical image applications, there is no need to completely fill the potential well because the photocurrent is a real-time response to the incident-light illumination. In other words, the readout can be done at any time of the integration process to reconstruct the incident signals. A longer integration time is not necessary unless a higher signal-to-noise ratio is needed. Indeed, a much shorter response time of approximately less than 1 μs can be achieved under fast-switching laser illumination (Fig. 2e), corresponding to a speed of >1 MHz. This speed is expected to be further improved by optimizing the contact and mobility of the SLG readout channel. Besides, we get a full well capacity of 1.8 Me$^-$ in the 5 μm × 5 μm (square) pixel, representing the maximum number of charges that the potential well can store. The noise power spectral density is shown in Supplementary Fig. 8, from which we calculate the noise equivalent power of 5.47 pW Hz$^{-1/2}$, and the extracted noise and corresponding dynamic range are 387 e$^-$ mm^{-2} and 73.4 dB, respectively. The noise in the GCI is expected to reduce further as the GCI can use the noise-cancelling circuit of CMOS-like correlated double sampling, due to its independent pixel structure.

Increasing imager bandwidth via charge injection. Another advantage of the GCI lies in its broadband response. Compared with traditional silicon CCDs where the detection wavelength is determined by the bandgap of silicon, the GCI can broaden the bandwidth by efficiently injecting hot carriers excited by IR light from MLG into silicon through the PTI effect (Fig. 1a,b). Here we use 40-nm-thick MLG, with weakly coupled graphene layers and over 40% light absorption from visible to MIR (Supplementary Fig. 1) to demonstrate the IR photocharge-injection effect. We use thin (200 μm) and low-doped (3 and 10 kΩ cm) silicon to increase the deep-depletion depth, leading to a shorter charge transport path from the MLG to the deep-depletion well (Supplementary Text 3 and Supplementary Fig. 16a). The long diffusion length of ~900 μm of low-doped wafer combined with the large depletion depth ensures most of the charges diffuse into the potential well once injected from the MLG into the silicon bottom surface (Supplementary Fig. 16). It should be noted that Supplementary Fig. 16a shows the measurement of diffusion length in the parallel direction near the surface. In fact, the diffusion length in the vertical direction can have a potentially longer value as the charge transport in the bulk is exposed to less scattering due to traps and dangling bonds than that of the surface. Direct measurements on the vertical diffusion length show it is longer than 700 μm in medium-doped silicon[41,42] and should be even longer in the low-doped silicon used here. The GCI shows pronounced response in the MIR region, as shown in the I_d–t curves under 3 μm laser illumination (Fig. 3a). The photon energy of the 3 μm illumination (~0.41 eV) is far below the bandgap of silicon (1.12 eV) and the barrier height of the MLG/Si junction (~0.49 eV; Supplementary Fig. 9 and Supplementary Text 7); therefore, the mechanism of intrinsic absorption in silicon and internal photoemission are ruled out. The MIR response is attributed to the hot carrier effect in the MLG. Graphitic materials are known to have strong carrier–carrier interactions due to the

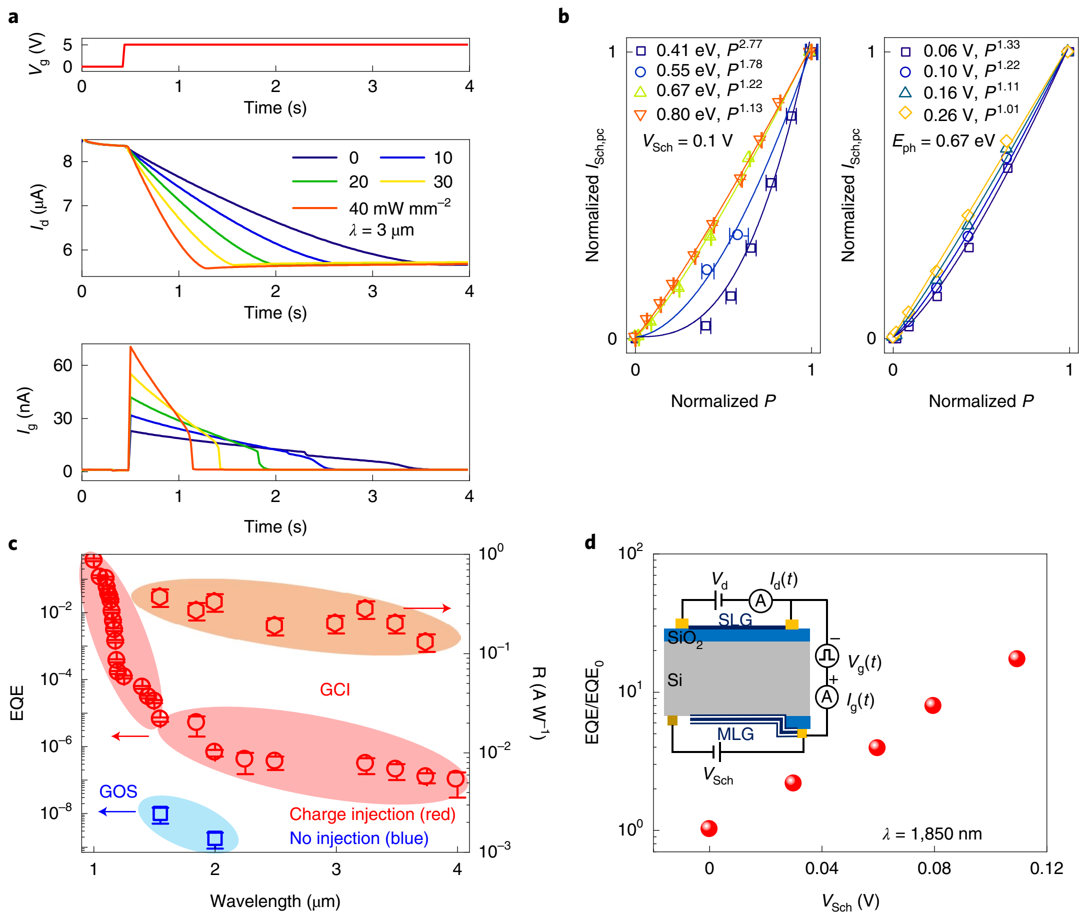

Fig. 3 | Characterization of GCI in the IR range. **a**, I_d–t and I_g–t curves of GCI under 3 μm laser illumination. **b**, Normalized photocurrent of MLG/Si junction as a function of illumination power at a constant bias (left) and constant photon energy (right). The lines are the fitting results with a power law $I_{Sch,pc} \approx P^{\gamma}$. The error bars are from deviations of multiple measurements. **c**, EQE and R of GCI (red) in the IR region and EQE of the control devices without charge injection (blue). The error bars are from the measurement error of laser power and laser-spot area, as well as deviation from the different batches of devices. **d**, EQE enhancement of the GCI under 1,850 nm laser illumination as a function of injection bias. The EQE_0 value is the EQE under zero external injection bias (V_{Sch}). Here V_{Sch} is applied to the MLG/Si Schottky junction to increase the hot-carrier injection efficiency. The inset shows a schematic of the GCI with an external injection bias.

weak screening of Coulomb potential[43]. Our MLG possesses a turbostratic stacking structure and is formed by weakly coupled graphene layers, as evident from the singlet 2D peak of the Raman spectrum (Supplementary Fig. 1). This indicates that our MLG retains the properties of the SLG due to its weak interlayer interaction[44,45]. The pump–probe data shows that the hot carrier lifetime is ~3 ps (Supplementary Fig. 1c), which demonstrates efficient hot carrier thermalization before the photocarriers lose energy to the lattice. From the superlinear dependence of the photocurrent ($I_{Sch,pc}$) on illumination power P, we verify that this long-wavelength light response is from the hot-carrier PTI effect (Fig. 3b). The photocurrent of the MLG/Si junction is fitted with a power law $I_{Sch,pc} \propto P^{\gamma}$, which shows a superlinear-to-linear transition when increasing the photon energy at a constant bias (Fig. 3b, left) and increasing the forward bias at a constant photon energy (Fig. 3b, right). γ is the fitted power law index. This is direct evidence that hot carrier thermalization and PTI emission effect dominate at longer wavelengths and in the low-bias region[34,46]. The nonlinearity in I_d–t and decreasing trend in I_g–t curves are due to the decrease in bias on the MLG/Si junction (Supplementary Fig. 10c). The deep-depletion region shrinks and V_g bias dropped on SiO_2 increases with time under illumination, which causes the decrease in bias dropped on the MLG/Si junction.

We summarize the EQE of our GCI in the IR region in Fig. 3c, from which two distinct regions are observed. The EQE first decreases as the wavelength increases from 1.0 to 1.2 μm, overlapping with the cutoff edge of silicon intrinsic absorption. The EQE gradually decreases when further increasing the incident wavelength up to 4 μm, which is beyond the bandgap absorption of silicon and barrier height of the MLG/Si junction ($2h\nu < \phi_h$). ϕ_h is the barrier height for holes. We attributed this photoresponse to the hot-carrier PTI emission mechanism with the evidence of superlinear power dependence (Fig. 3b). The control experiments of IR absorption in silicon are demonstrated using the SLG/SiO_2/Si (GOS) structure without a charge-injection layer (Fig. 3c (blue squares) and Supplementary Fig. 11). Compared with the GOS structure without the charge-injection function, the spectral bandwidth of GCI is notably extended and the EQE has been improved by two orders of magnitude. Currently, the EQE in the IR region is limited by the low charge-injection efficiency, which is attributed to the high Schottky barrier height in the MLG/Si junction. Instead of conducting majority carriers under a reverse bias as in traditional Schottky diodes, the MLG/Si in our GCI works with minority carriers (holes in n-type silicon) dominated under an open-circuit forward bias. A moderate forward bias is expected to decrease the barrier height for holes; however, in GCI, only a small forward bias can be obtained because most of the V_g bias is dropped on the deep-depletion region and SiO_2 layer. To improve the charge-injection efficiency, we apply external injection bias (V_{Sch}) on the MLG/Si Schottky junction (Fig. 3d). The EQE increases exponentially as V_{Sch} increases and can be improved by one order of magnitude within an injection bias of 0.1 V. Although the EQE of GCI in the IR region is lower than that in the visible region, we can obtain considerable responsivity in the IR region due to the large transconductance gain in the GCI. For instance, the responsivity exceeds 0.1 A W^{-1} in the IR region, which outperforms many other state-of-the-art image sensors (Fig. 3c and Supplementary Table 1). The responsivity slowly decreases as the incident wavelength increases (Supplementary Text 5).

Mechanism of GCI. In our device, the PTI emission allows a high Schottky barrier between the MLG and silicon that suppresses the thermal noise—the main limiting factor for room-temperature operation in traditional IR photodetectors. Although the high barrier results in a lower quantum efficiency, the synergetic combination of PTI, charge integration and transconductance amplification provides a large responsivity that is initially compromised for lower noise in our device structure. The superlinear relationship of $I_{Sch,pc} \approx P^{\gamma}$ (Fig. 3b) and tunable EQE by V_{Sch} (Fig. 3d) are two direct evidences that hot-carrier PTI emission from the MLG to silicon dominates the IR response. In addition, we exclude the contribution of heat from various factors. First, heating in SLG and MLG can lead to the bolometric effect. In SLG, an increase in resistance under IR laser illumination results in a negative photocurrent (Supplementary Fig. 11d), a typical feature of the bolometric effect[47]. However, the responsivity from the bolometric effect is much lower (approximately five orders of magnitude) than the response observed from the photocharge-injection effect (2.0 μA W^{-1} of the bolometric effect of SLG (Supplementary Fig. 11d) and 0.6 A W^{-1} of photocharge-injection effect (Fig. 3c)). Besides, other thermal effects that could lead to the change in mobility of MLG cannot translate into a response in the SLG channel and thus can be ruled out. The heat transfer from the MLG to silicon and the consequent thermal carrier generation and integration in the deep-depletion well of silicon can also be excluded. Such a heat transfer effect is not controlled by the external voltage, contrary to that observed in Fig. 3d. We also considered the heat effects in the silicon substrate. In principle, thermally generated carriers in silicon integrate in the deep-depletion well that reflects in the channel current I_d of graphene. However, the negligible IR response in the GOS structure without MLG on the bottom silicon surface excludes the heat effect from silicon (Supplementary Fig. 11). Since the hot electron generation and transport in MLG play key roles in IR detection via the PTI effect in our device, the photothermoelectric (PTE) effect can also be expected in MLG. The PTE effect in MLG emerges from the electron temperature gradient that transport hot electrons towards the heat sink or the junction. Considering the thickness of MLG, the PTE effect is primarily influenced by the interlayer hot-electron transfer rather than the Seebeck coefficient in MLG[48]. As a result, hot electrons distribute into a wider area of MLG and thus helps to enhance the PTI effect at the MLG/Si junction, contributing to the charge-injection process. Besides, MLG could produce a small resistive change under light illumination and change the back-gate voltage accordingly, contributing to the photoresponse. However, this resistive change is too small to produce a detectable photoresponse even under large transconductance gain as a very little V_g drops on the MLG; thus, it cannot dominate the photoresponse in our devices. The photoresponse from surface-state absorption can also be eliminated in the MIR region as our control reference devices show a weak response (Supplementary Fig. 11).

We observed from the TEM (Fig. 1f) that an ~2 nm native oxide exists between the MLG and silicon and could act as a tunnel barrier for the hot carriers. This native oxide layer is too thin to block the current conduction, where the charge carriers can transport through the ~2 nm native oxide by direct tunnelling. Our MLG/Si junction shows a typical rectification feature and good conduction under forward bias (Supplementary Fig. 10d). The native oxide may slightly modify the properties of the barrier in two ways. First, the native oxide as a barrier could block some of the photocarriers, especially for those with lower energies. In this case, the blocked photocarriers have a higher chance to participate in the carrier–carrier scattering in the MLG and contribute to the PTI effect[46]. On the other hand, the portion of thermalized carriers with lower energy can have a slightly smaller tunnelling probability and are more likely to lose energy to the lattice. This could reduce the charge-injection efficiency and current density in the MLG/Si junction if the native oxide is thick. Besides, the native oxide could suppress the reverse leakage current of the junction by reducing the interfacial recombination due to interface or surface states[49]. The existence of the native oxide layer could increase the chance of impact ionization inside the oxide layer and impact ionization of hot carriers emitted from the MLG, which is expected to contribute to the large responsivity in the longer-wavelength region[50–52].

The construction of GCI allows us to achieve broadband imaging (Supplementary Fig. 13). A proof-of-concept linear array is constructed to demonstrate the potential of the GCI pixels for scalable integration. Importantly, with GCIs, broadband images can be reconstructed under ambient light, ultraviolet (375 nm), NIR (1,342 nm) and MIR (3.0 and 3.8 μm), respectively, based on a single-pixel scanning method (Methods and Supplementary Text 10). The scanning methods for the single pixel and linear array are shown in Supplementary Fig. 13. The intensity and contrast of both visible and IR images increase with the integration time. The long integration time is important to improve the image quality, especially for the low-light-level condition or MIR regime, where the responsivity is lower. With an independent pixel structure and real-time readout, the GCI shows an excellent anti-blooming effect that was a common challenge in traditional CCDs[53]. To obtain high-resolution images, the pixel size can be scaled down to as small as 5 μm, which is at the level of the incident wavelength. The performance such as conversion gain and responsivity are improved at a smaller pixel size (Fig. 2g). We note that the high dark current may become a drawback for the device in real applications. Although the graphene readout channel offers high responsivity, high speed and high linearity, it leads to a higher dark current and power consumption. This power consumption can be reduced by reducing V_d with high signal-to-noise-ratio circuits, as reported before[22]. The power-consumption performance is expected to be further improved by replacing graphene with semiconducting transition metal dichalcogenides as they offer a lower dark current. The constructed images demonstrate the potential of our device for broadband imaging based on single pixels. In real imagers, on-chip circuits and a pixel array with a small pitch are necessary. Several circuit and isolation technologies (Supplementary Fig. 12) are expected to promote the potential of our device in real applications in the future. The on-chip readout circuits can be manufactured on the same wafer with the pixel array[22] (Supplementary Fig. 12a,b). The processing of the backside MLG and back gate can adopt the mature backside-illuminated image sensor technology, which has high compatibility with current CMOS processes[54]. Deep trench isolation is expected to be used to eliminate crosstalk among adjacent pixels (Supplementary Fig. 12c–e). These circuits and integration methods have high compatibility with current CMOS technologies and may help accelerate the progress of our GCI photodetectors towards real applications.

Conclusions

We have reported GCI photodetectors consisting of a silicon deep-depletion well for charge integration, a top SLG layer for non-destructive direct readout and a bottom MLG layer for photocharge injection. The silicon absorbs visible light and the MLG mainly absorbs IR light, broadening the bandwidth of the photodetector to the MIR regime. It should be noted that the GCI can potentially work at longer wavelengths beyond 4 μm, as the photoresponse depends on the hot carrier temperature in the MLG and is limited neither by the bandgap of silicon nor the barrier height of the MLG/Si Schottky junction. In addition to MLG, other materials such as platinum silicide alloy[16,17] are potential candidates for broadband detection in the GCI. The spectral performance can be optimized by using various materials as the charge-injection layer.

The GCI photodetector combines features such as broadband response, direct readout, high room-temperature sensitivity (above 0.1 A W^{-1} in the IR regime and 6×10^4 A W^{-1} in the visible regime), fast response (<1 μs) and low-cost implementation. Due to the slow thermal carrier generation rate in silicon, GCI can perform the function of pixel information storage via the storage of light-induced carriers in the potential well. Combined with tunable responsivity, which can be used as the weight, the GCI can be potentially used to build neuromorphic networks. The combination of charge injection, integration and direct independent readout in each pixel could be used to make new imaging devices with applications in various fields.

Methods

Device fabrication. The devices were fabricated on commercially available lightly doped n-type Si wafer (thickness, 200 μm; double-side polished) with a 15 or 100 nm thermal SiO_2 layer. The resistivity of the wafer is 3 or 10 kΩ cm for all the IR tests. In the test in the visible spectral range, the resistivity of both 1–10 Ω cm and 10 kΩ cm are used, and similar performance is obtained. The fabrication process is as follows:

(1) Formation of top and bottom metal electrodes: photolithography followed by electron-beam deposition and liftoff were used to deposit the electrodes (Au/Cr, 50/5 nm) on the top side of the wafer. Then, bottom-side-alignment lithography as well as electron-beam deposition and liftoff were conducted to deposit electrodes on the bottom side of the wafer.
(2) CVD SLG transfer and pattern: CVD graphene was transferred onto the patterned electrodes using a wet etching method[55]. The graphene was patterned using a photolithography process and etched by O_2 plasma.
(3) Si window at bottom side: photolithography at the bottom side and subsequent etching with buffered oxide etchant were conducted to open a SiO_2 window in the device area.
(4) Bottom MLG transfer and patterning: MLG was directly transferred onto the bottom electrodes with the assistance of ethyl alcohol. Then, photolithography and inductively coupled plasma etching (Oxford Plasmalab System 100) were used to pattern the MLG.

Finally, the devices were treated with fast annealing (400 °C, 5 min) to improve contact between the graphene and Si and remove the residuals.

Preparation of MLG. To fabricate the graphene oxide (GO) membranes with a uniform structure, a diluted GO solution with a concentration of 4 μg l^{-1} was filtrated under a vacuum by anodic aluminium oxide (AAO) filters (Whatman; pore size, 0.2 μm; diameter, 48 mm). After filtration, the GO/AAO membrane was reduced by HI vapour for 8 h in a sealed container heated under 100 °C. Then, the obtained reduced graphene oxide (rGO)/AAO membrane was placed above a bottle (diameter, 48 mm) containing camphor, with the GO side facing the camphor. The bottom of the bottle was then heated to 120–200 °C to deposit the camphor (10–50 mg) on the surface of the rGO film. After 3–10 min, the camphor/rGO/AAO membrane was slowly moved into room temperature and the camphor/rGO film automatically separated from the AAO membrane. Then, a continuous heating process (60 °C) was used to remove the camphor, leaving a freestanding rGO film. Finally, the freestanding rGO film was further heated to 2,000 °C at 10 °C min^{-1} and held for 8 h to heal most of the defects on it, and then heated to 2,300 °C at 100 °C min^{-1} and held for 1 min to remove the residue defects on it in a high-temperature graphite furnace (NTG-SML-50L, Changsha Nuotian Electronic Technology) protected by Ar (ref. [56]).

Electrical and optoelectrical measurements. The electrical measurements were accomplished by a semiconductor analyser (Agilent B1500A) and Capacitance-Voltage (CV) data were measured by an LCR meter (TH2828). For the pulse testing, we used a two-channel signal generator (RIGOL DG1000Z) and a voltage amplifier (Falco Systems WMA-300) to generate the voltage pulses. For the pulsed laser testing, the laser was modulated by the signal generator and synchronized with the gate-voltage pulse. For optoelectrical testing, light was illuminated from the top side of the device. Visible and NIR light were provided by three kinds of light sources: lasers (375, 532, 633, 1,342, 1,550 and 1,850 nm), incandescent lamp and Xe lamp with a colour filter (~300–1,200 nm). The power of these light sources was measured by commercial Si (Thorlabs S120VC) and InGaAs (Thorlabs S184C) photodetectors. MIR (2–4 μm, ~200 fs, 76 MHz repetition rate) light was provided by a mode-locked Ti:sapphire laser (Coherent, Mira-HP) with synchronously pumped optical parametric oscillator. The pulse energy used in the measurements (~0.1–0.5 nJ) is below the threshold of the multiphoton absorption of Si (refs. [57,58]). Two IR band-pass filters (FB2000-500 to FB4000-500, Thorlabs) were used in series to filter out the stray light from the MIR laser. A calcium fluoride aspherical lens was used to focus the IR light on the device. The power was measured by a thermopile detector (Newport 1918-R). For the photograph, we built a scanning system with a focused laser and programmable X–Y stage. A data acquisition card was used to obtain the I_d–t data.

SEM, TEM and Raman data. SEM images were obtained using a Hitachi S4800 field-emission microscope at an acceleration voltage of 5 kV. The TEM samples were prepared using the in situ focused ion beam (FIB) technique on an FEI Strata 400 dual-beam FIB/SEM. The samples were capped with sputtered C and Pt electrode by the focused electron/ion beam (e-Pt/I-Pt) before milling. The images were obtained with an FEI Tecnai Osiris FEG/TEM operated at 300 kV in the bright-field TEM mode and high-resolution TEM mode. Raman spectroscopy was measured using a confocal Raman microscope (Senterra, Bruker) and a Renishaw Invia system. The excitation wavelength was 532 nm.

Data availability

Source data are provided with this paper. The data that support the other findings of this study are available from the corresponding authors upon reasonable request.

Received: 7 November 2020; Accepted: 23 March 2022;
Published online: 02 May 2022

References

1. Boyle, W. S. & Smith, G. E. Charge coupled semiconductor devices. *Bell Syst. Tech. J.* **49**, 587–593 (1970).
2. Amelio, G. F. et al. Experimental verification of the charge coupled device concept. *Bell Syst. Tech. J.* **49**, 593–600 (1970).
3. Smith, G. E. Nobel lecture: the invention and early history of the CCD. *Rev. Mod. Phys.* **82**, 2307–2312 (2010).
4. Nakata, S. et al. A wearable pH sensor with high sensitivity based on a flexible charge-coupled device. *Nat. Electron.* **1**, 596–603 (2018).
5. Zhang, H.-F. et al. Scientific CCD camera for the CSTAR2 telescope in Antarctica. *J. Astron. Telesc. Instrum. Syst.* **5**, 036002 (2019).
6. Tiffenberg, J. et al. Single-electron and single-photon sensitivity with a silicon skipper CCD. *Phys. Rev. Lett.* **119**, 131802 (2017).
7. Murata, M. et al. A 24.3 Me⁻ full well capacity CMOS image sensor with lateral overflow integration trench capacitor for high precision near infrared absorption imaging. in *2018 IEEE International Electron Devices Meeting (IEDM)* 10.3.1–10.3.4 (IEEE, 2018).
8. Kim, W.-T. et al. A high full well capacity CMOS image sensor for space applications. *Sensors* **19**, 1505 (2019).
9. Durini, D. & Arutinov, D. in *High Performance Silicon Imaging* 2nd edn (ed Durini, D.) 25–73 (Woodhead Publishing, 2020).
10. Magnan, P. Detection of visible photons in CCD and CMOS: a comparative view. *Nucl. Instrum. Methods Phys. Res. A* **504**, 199–212 (2003).
11. Luštica, A. CCD and CMOS image sensors in new HD cameras. in *Proc. ELMAR-2011* 133–136 (IEEE, 2011).
12. Marcelot, O. et al. Study of CCD transport on CMOS imaging technology: comparison between SCCD and BCCD, and ramp effect on the CTI. *IEEE Trans. Electron Devices* **61**, 844–849 (2014).
13. Gamal, A. E. & Eltoukhy, H. CMOS image sensors. *IEEE Circuits Devices Mag.* **21**, 6–20 (2005).
14. Suzuki, M. et al. An over 1Mfps global shutter CMOS image sensor with 480 frame storage using vertical analog memory integration. in *2016 IEEE International Electron Devices Meeting* 8.5.1–8.5.4 (IEEE, 2016).
15. Bigas, M. et al. Review of CMOS image sensors. *Microelectron. J.* **37**, 433–451 (2006).
16. Shepherd, F. D. & Yang, A. C. Silicon Schottky retinas for infrared imaging. in *International Electron Devices Meeting* 310–313 (IEEE, 1973).
17. Yutani, N. et al. 1040*1040 element PtSi Schottky-barrier IR image sensor. in *International Electron Devices Meeting 1991* 175–178 (IEEE, 1991).
18. Denda, M. et al. 4-band*4096-element Schottky-barrier infrared linear image sensor. *IEEE Trans. Electron Devices* **38**, 1131–1135 (1991).
19. Leitz, C. et al. Development of germanium charge-coupled devices. in *Proc. SPIE 10709 High Energy, Optical, and Infrared Detectors for Astronomy VIII* 1070908 (International Society for Optics and Photonics, 2018).

20. Manda, S. et al. High-definition visible-SWIR InGaAs image sensor using Cu-Cu bonding of III-V to silicon wafer. in *2019 IEEE International Electron Devices Meeting (IEDM)* 16.7.1–16.7.4 (IEEE, 2019).
21. Wang, Y. et al. Fast uncooled mid-wavelength infrared photodetectors with heterostructures of van der Waals on epitaxial HgCdTe. *Adv. Mater.* **34**, 2107772 (2022).
22. Goossens, S. et al. Broadband image sensor array based on graphene–CMOS integration. *Nat. Photon.* **11**, 366–371 (2017).
23. Akinwande, D. et al. Graphene and two-dimensional materials for silicon technology. *Nature* **573**, 507–518 (2019).
24. Kong, W. et al. Path towards graphene commercialization from lab to market. *Nat. Nanotechnol.* **14**, 927–938 (2019).
25. Zhu, Y. et al. Mass production and industrial applications of graphene materials. *Natl Sci. Rev.* **5**, 90–101 (2017).
26. Howell, S. W. et al. Graphene-insulator-semiconductor junction for hybrid photodetection modalities. *Sci. Rep.* **7**, 14651 (2017).
27. Ruiz, I. et al. Interface defect engineering for improved graphene-oxide-semiconductor junction photodetectors. *ACS Appl. Nano Mater.* **2**, 6162–6168 (2019).
28. Liu, C.-H. et al. Graphene photodetectors with ultra-broadband and high responsivity at room temperature. *Nat. Nanotechnol.* **9**, 273–278 (2014).
29. Chen, X. et al. Graphene hybrid structures for integrated and flexible optoelectronics. *Adv. Mater*. **32**, 1902039 (2019).
30. Bao, Q. & Loh, K. P. Graphene photonics, plasmonics, and broadband optoelectronic devices. *ACS Nano* **6**, 3677–3694 (2012).
31. Zhang, B. Y. et al. Broadband high photoresponse from pure monolayer graphene photodetector. *Nat. Commun.* **4**, 1811 (2013).
32. Yu, X. et al. A high performance, visible to mid-infrared photodetector based on graphene nanoribbons passivated with HfO_2. *Nanoscale* **8**, 327–332 (2016).
33. Yu, X. et al. Narrow bandgap oxide nanoparticles coupled with graphene for high performance mid-infrared photodetection. *Nat. Commun.* **9**, 4299 (2018).
34. Massicotte, M. et al. Photo-thermionic effect in vertical graphene heterostructures. *Nat. Commun.* **7**, 12174 (2016).
35. Liu, Y. et al. Van der Waals integration before and beyond two-dimensional materials. *Nature* **567**, 323–333 (2019).
36. Wang, Y. et al. Van der Waals contacts between three-dimensional metals and two-dimensional semiconductors. *Nature* **568**, 70–74 (2019).
37. Shimatani, M. et al. Giant Dirac point shift of graphene phototransistors by doped silicon substrate current. *AIP Adv.* **6**, 035113 (2016).
38. Guo, X. et al. High-performance graphene photodetector using interfacial gating. *Optica* **3**, 1066–1070 (2016).
39. Zhou, F. et al. Optoelectronic resistive random access memory for neuromorphic vision sensors. *Nat. Nanotechnol.* **14**, 776–782 (2019).
40. Adinolfi, V. & Sargent, E. H. Photovoltage field-effect transistors. *Nature* **542**, 324–327 (2017).
41. Ioannou, D. E. & Dimitriadis, C. A. A SEM-EBIC minority-carrier diffusion-length measurement technique. *IEEE Trans. Electron Devices* **29**, 445–450 (1982).
42. Castaldini, A. et al. Determination of bulk and surface transport properties by photocurrent spectral measurements. *Appl. Phys. A* **71**, 305–310 (2000).
43. Tan, S. et al. Ultrafast multiphoton thermionic photoemission from graphite. *Phys. Rev. X* **7**, 011004 (2017).
44. Berashevich, J. & Chakraborty, T. Interlayer repulsion and decoupling effects in stacked turbostratic graphene flakes. *Phys. Rev. B* **84**, 033403 (2011).
45. Shallcross, S. et al. Electronic structure of turbostratic graphene. *Phys. Rev. B* **81**, 165105 (2010).
46. Ma, Q. et al. Tuning ultrafast electron thermalization pathways in a van der Waals heterostructure. *Nat. Phys.* **12**, 455–459 (2016).
47. Yuan, S. et al. Room temperature graphene mid-infrared bolometer with a broad operational wavelength range. *ACS Photonics* **7**, 1206–1215 (2020).
48. Fang, B. et al. Bidirectional mid-infrared communications between two identical macroscopic graphene fibres. *Nat. Commun.* **11**, 6368 (2020).
49. Xu, J. et al. Ultra-broadband graphene-InSb heterojunction photodetector. *Appl. Phys. Lett.* **111**, 051106 (2017).
50. Yin, J. et al. Engineered tunneling layer with enhanced impact ionization for detection improvement in graphene/silicon heterojunction photodetectors. *Light Sci. Appl.* **10**, 113 (2021).
51. Zhu, H. et al. Metal–oxide–semiconductor-structured MgZnO ultraviolet photodetector with high internal gain. *J. Phys. Chem. C* **114**, 7169–7172 (2010).
52. Wang, W. J. et al. Metal–insulator–semiconductor–insulator–metal structured titanium dioxide ultraviolet photodetector. *J. Phys. D: Appl. Phys.* **43**, 045102 (2010).
53. Janesick, J. R. Scientific charge-coupled devices. *Opt. Eng.* **26**, 268692 (2001).
54. Lahav, A. et al. in *High Performance Silicon Imaging* 2nd edn (ed Durini, D.) 95–117 (Woodhead Publishing, 2020).
55. Wan, X. et al. A self-powered high-performance graphene/silicon ultraviolet photodetector with ultra-shallow junction: breaking the limit of silicon? *npj 2D Mater. Appl.* **1**, 4 (2017).
56. Peng, L. et al. Multifunctional macroassembled graphene nanofilms with high crystallinity. *Adv. Mater.* **33**, 2104195 (2021).
57. Grojo, D. et al. Long-wavelength multiphoton ionization inside band-gap solids. *Phys. Rev. B* **88**, 195135 (2013).
58. Briggman, K. A. et al. Imaging and autocorrelation of ultrafast infrared laser pulses in the 3–11-μm range with silicon CCD cameras and photodiodes. *Opt. Lett.* **26**, 238–240 (2001).

Acknowledgements

We thank C. Jin and X. Zhang for help on the NIR test and L. Chen and H. Zhu for help on the MIR test. We thank E. Li, W. Yin, D. Dai, W. Chen, K. Huang, Z. Tan, H. Shen, C. Li, S. Song, Q. Xiong and T. Low for valuable discussions. Y.X. acknowledges the support of this work by NSFC (grant nos.92164106, 61874094, 62090030 and 52090030); the Fundamental Research Funds for the Central Universities (K20200060 and 2021FZZX001-17); ZJU Micro-Nano Fabrication Center.

Author contributions

Y.X., H.G. and X.D. designed the research. Y.X., H.G., W. L. and J.L. designed the experiment. L.P. and C.G. synthesized the MLG and developed the transfer methods. K.L. synthesized the SLG. Y.X., W.L., J.L., C.L. and Y.L. fabricated the devices and carried out the measurements. Y.X., L. Liu and L. Li assisted in part of the experiment. Y.X., H.G., P.W., S.C.B., K.S., Z.S., T.H. and B.Y. helped improve the manuscript. Y.X., X.W., C.G., B.Y., and X.D. guided the project. All the authors contributed to interpreting the data and writing the manuscript.

Competing interests

The authors declare no competing interests.

Additional information

Supplementary information The online version contains supplementary material available at https://doi.org/10.1038/s41928-022-00755-5.

Correspondence and requests for materials should be addressed to Yang Xu, Xiaomu Wang, Chao Gao, Bin Yu or Xiangfeng Duan.

Peer review information *Nature Electronics* thanks Lukas Mennel and the other, anonymous, reviewer(s) for their contribution to the peer review of this work.

Reprints and permissions information is available at www.nature.com/reprints.

Publisher's note Springer Nature remains neutral with regard to jurisdictional claims in published maps and institutional affiliations.

© The Author(s), under exclusive licence to Springer Nature Limited 2022